



Research paper

Comparison of importance between separation efficiency and valence band position: The case of heterostructured $\text{Bi}_3\text{O}_4\text{Br}/\alpha\text{-Bi}_2\text{O}_3$ photocatalysts

Jian-guo Guo, Ying Liu, Ying-juan Hao, Yi-lei Li, Xiao-jing Wang, Rui-hong Liu, Fa-tang Li*

College of Science, Hebei University of Science and Technology, Shijiazhuang, 050018, China



ARTICLE INFO

Keywords:

$\text{Bi}_3\text{O}_4\text{Br}$
 $\alpha\text{-Bi}_2\text{O}_3$
 Valence band position
 Separation efficiency
 Heterojunction

ABSTRACT

Heterostructured $\text{Bi}_3\text{O}_4\text{Br}/\alpha\text{-Bi}_2\text{O}_3$ nanocomposites are prepared via *in situ* one-step self-combustion of ionic liquids. Tetrabutylammonium bromide (TBAB) is employed to be fuel, complexing agent for ionic liquids, as well as the reactant supplying Br for the objective material. The ratio of $\text{Bi}_3\text{O}_4\text{Br}/\alpha\text{-Bi}_2\text{O}_3$ can be easily adjusted by controlling the amount of TBAB. The heterojunctions show higher photocatalytic ability towards both azo dye methyl orange (MO) and colorless pollutant phenol. The electron spin resonance (ESR) test and p-nitro blue tetrazolium chloride (NBT) degradation result indicate that generation amounts of superoxide anion radicals ($\cdot\text{O}_2^-$) over heterojunctions are less than that over pure $\text{Bi}_3\text{O}_4\text{Br}$. Photoelectrochemical measurements show that separation efficiencies of photo-generated electrons and holes are decreased after the combination of $\text{Bi}_3\text{O}_4\text{Br}$ and $\alpha\text{-Bi}_2\text{O}_3$. Work function test and scavenger experiments display that holes play key role for pollutant degradation and the position of holes on $\alpha\text{-Bi}_2\text{O}_3$ is lowered via hybridization. Thus, the enhanced photocatalytic activity over composites can be attributed to the position decline of $\alpha\text{-Bi}_2\text{O}_3$ valence band, thus improving the reactivity of holes in direct oxidation of pollutants. In this case, valence band position is confirmed to be more important than separation efficiency of charge carriers in affecting photocatalytic performance.

1. Introduction

With the rapid progress of industrialization, human beings have been seriously obsessed by environmental pollution issues. Photocatalytic oxidation with semiconductors, as a promising environmental purification technology, has attracted tremendous attentions in wastewater remediation and other environment governance [1,2]. Undoubtedly, developing photocatalyst materials is the premise of the photocatalytic technology for practical application. In recent decades, people have made great efforts to develop visible-light-driven photocatalysts because traditional photocatalysts such as TiO_2 and ZnO can only harvest the UV-light that just accounts for 3–5% of solar energy owing to their large energy band gaps (3.0–3.2 eV) [3–5]. Graphitic Carbon Nitride ($\text{g-C}_3\text{N}_4$) is a typical representative of novel photocatalyst since Wang et al. [6] reported its excellent activity in water splitting. However, because of its high position of highest occupied molecular orbital (HOMO), it is difficult to realize fully mineralization of organic pollutants over $\text{g-C}_3\text{N}_4$.

Bismuth-based semiconductors, such as Bi_2O_3 , BiOBr , BiOI , BiVO_4 , Bi_2WO_6 , are low-cost, eco-friendly and high-efficiency visible-light photocatalysts and have been widely applied for organic pollutants degradation, H_2 generation, and CO_2 reduction [1,2,7–14]. To further

overcome the drawback that single component photocatalysts have low separation efficiency of photoinduced carriers, one mostly employed strategy is to construct heterojunctions by coupling two or more semiconductors, such as $\text{BiOBr}/\text{Bi}_2\text{WO}_6$ [2], $\text{TiO}_2/\text{BiOBr}$ [15], $\text{Bi}_2\text{MoO}_6/\text{TiO}_2$ [16], $\text{BiVO}_4/\text{TiO}_2$ [17], $\text{Pd}/\text{BiVO}_4/\text{BiOBr}$ [18], $\text{Bi}_2\text{O}_3/\text{Bi}_2\text{WO}_6$ [19], $\text{BiVO}_4/\beta\text{-Bi}_2\text{O}_3$ [20], $\text{BiPO}_4/\text{BiOI}$ [21]. The results indicate that it is really an effective approach because of the efficient transfer of charge carriers between/among the counterparts of heterojunction. However, there are still issues around the heterostructured photocatalysts. For example, does heterojunction formation surely result in the enhancement of separation efficiency of photo-induced carriers? Can we evaluate the efficacy between heterojunction construction and other strategies directly?

On the other hand, from the point of the view of reaction mechanism, it is commonly known that the active species including superoxide anion radicals ($\cdot\text{O}_2^-$), hydroxyl radicals ($\cdot\text{OH}$), and hole (h^+) exert decisive role in the photocatalytic degradation process of organic pollutants [22,23]. Among them, $\cdot\text{OH}$ is generally considered as the most efficient active oxidant responsible for the oxidative reactions, which is derived from the interaction between h^+ and H_2O adsorbed on the surface of catalysts [24]. However, as for bismuth-based photocatalysts, it is almost impossible to produce $\cdot\text{OH}$ because that the

* Corresponding author.

E-mail address: lifatang@126.com (F.-t. Li).

standard redox potential of $\text{Bi}^{\text{V}}/\text{Bi}^{\text{II}}$ ($E^{\circ} = 1.59 \text{ V}$ at pH 0) is less than that of $\cdot\text{OH}/\text{H}_2\text{O}$ (2.27 V versus the standard hydrogen electrode (SHE)) [25,26] and $\cdot\text{OH}/\text{OH}^-$ (1.99 V) [27]. Therefore, the active role of holes should be paid more attention in Bi-based photocatalysis systems.

It is known that the oxidizing capability of photogenerated holes directly hinges on the location of VB [28]. The more positive valence band position, the stronger oxidation ability of holes is. Hence, it should be an effective route to raise the capacity of photocatalytic oxidation by moving down the location of VB. Nevertheless, to our knowledge, no systematic study concerning the mediation of a valence band has been published yet; on the contrary, much attention has been devoted to the separation efficiency of photogenerated charges. Considering that both VB position and separation efficiency have a significant effect on the enhanced photocatalytic ability, we design a novel heterojunction to investigate which factor is more efficient and plays a momentous guiding role on the design of photocatalysts.

Bismuth oxybromide (BiOBr) has layered structure and desirable band gap of about 2.7 eV that lead to excellent photocatalytic performance [29,30]. As members of BiOBr family, bromide-poor type photocatalysts, such as $\text{Bi}_3\text{O}_4\text{Br}$ [31], $\text{Bi}_{24}\text{O}_{31}\text{Br}_{10}$ [32], have more excellent visible-light absorption performance and much lower combination rate of photo-induced electrons and holes than pristine BiOBr . In this paper, the $\text{Bi}_3\text{O}_4\text{Br}/\alpha\text{-Bi}_2\text{O}_3$ heterojunctions were constructed for the first time via one-step ionic liquid self-combustion route developed by our group [33,34]. This solution combustion method can ensure the formation of homogeneous solution of precursors in atomic scale and thus good contact between the components of hybrids [35]. The formation of this heterojunction result in the down of VB position and the decrease of separation efficiency of photo-induced carriers, and subsequently the determining factor responsible for photocatalytic activity is discussed by means of investigating the band energy structures, electrochemical properties, surface photovoltages, and work functions of the as-prepared photocatalysts. Finally, a possible degradation mechanism for the enhanced photocatalytic performance is proposed.

2. Experimental section

2.1. Chemicals and catalysts preparation

Tetrabutylammonium bromide ($(\text{C}_4\text{H}_9)_4\text{NBr}$, TBAB, 99%) was obtained from Aladdin Reagents Co. Ltd (Shanghai, China), and the bismuth nitrate pentahydrate ($\text{Bi}(\text{NO}_3)_3 \cdot 5\text{H}_2\text{O}$, AR), urea ($\text{CO}(\text{NH}_2)_2$, AR), methyl orange (MO, AR), phenol (AR), and ethylene glycol (EG, AR) were purchased from Sinopharm (Shanghai, China). All of the chemicals were used as received without further purification.

For synthesizing $\text{Bi}_3\text{O}_4\text{Br}$, 0.0050 mol $\text{Bi}(\text{NO}_3)_3 \cdot 5\text{H}_2\text{O}$ mixed with 0.0017 mol TBAB and 0.0015 mol urea were dissolved in 10 mL of EG, and then the mixture was heated on an electric furnace until the formation of a white solution, which is an ionic liquid (IL, $[(\text{C}_4\text{H}_9)_4\text{N}]^+[\text{Bi}(\text{NO}_3)_3\text{Br}]^-$). Afterwards, the IL was moved into a tube furnace maintained at $300 \text{ }^\circ\text{C}$ and heated at a heating rate of $20 \text{ }^\circ\text{C min}^{-1}$ with a O_2 flow rate of 800 mL min^{-1} . Finally, the $\text{Bi}_3\text{O}_4\text{Br}$ was obtained when the combustion process was finished accompanying the emission of a large amount of gas. $\text{Bi}_3\text{O}_4\text{Br}/\alpha\text{-Bi}_2\text{O}_3$ hybrids with different proportions can

be acquired by simply adjusting the ratio of $\text{Bi}(\text{NO}_3)_3 \cdot 5\text{H}_2\text{O}$ and TBAB. The designed various ratios of $\text{Bi}_3\text{O}_4\text{Br}/\alpha\text{-Bi}_2\text{O}_3$ are listed in Table 1, which are denoted as XBB (X represents the weight ratio of $\text{Bi}_3\text{O}_4\text{Br}$ to $\alpha\text{-Bi}_2\text{O}_3$). For comparison, pure $\alpha\text{-Bi}_2\text{O}_3$ sample was obtained by burning 0.0051 mol $\text{Bi}(\text{NO}_3)_3 \cdot 5\text{H}_2\text{O}$ and 0.0102 mol urea.

2.2. Catalyst characterization

To determine the crystal phases and their composition, X-ray diffraction (XRD) was recorded on a Rigaku D/MAX 2500 X-ray diffractometer. The morphology of the as-prepared samples were observed by means of a Hitachi S4800 field-emission scanning electron microscope (FE-SEM). High-resolution transmission electron microscopy (HRTEM) images were acquired by a JEOL JEM-2100 electron microscope. N_2 adsorption/desorption measurements were carried out on Micromeritics Tristar II 3020 apparatus. The UV-vis diffuse reflectance spectra (DRS) were obtained using Thermo Scientific Evolution 220 spectrophotometer to investigate the optical absorption property. Time-resolved photoluminescence (PL) spectroscopy was recorded on an FS5 Fluorescence spectrometer (Edinburgh Instruments) with an excitation source at 310 nm. X-ray photoelectron spectroscopy (XPS) measurements were performed on a PHI 1600 ESCA XPS system. Electron spin resonance (ESR) spectra were collected using a Bruker EMX-8/2.7 X-band ESR spectrometer to observe the active species generated in the photocatalytic process. O_2 temperature programmed desorption ($\text{O}_2\text{-TPD}$) was performed on Beijing BUILDER PCA-1200 Chemisorption analyzer. The $\text{O}_2\text{-TPD}$ curves were obtained by gradually increasing the temperature to $600 \text{ }^\circ\text{C}$ with a ramping rate of $10 \text{ }^\circ\text{C min}^{-1}$.

2.3. Photocatalytic activity tests

The photocatalytic performances of the samples were obtained by degrading methyl orange (MO, 10 mg/L) and phenol (50 mg/L). Firstly, 100 mg of photocatalyst was put into 100 mL of the pollutant solution under magnetically stirring in darkness for 0.5 h to reach the adsorption/desorption equilibrium. Subsequently the mixture was irradiated by a 350 W Xe lamp with a 400 nm cut-off filter as the visible-light source. During the photocatalytic process, 2 mL of the suspension was taken at fixed intervals and centrifuged to monitor the pollutant concentrations using a Thermo Scientific Evolution 220 UV-vis spectrophotometer at their maximum absorption wavelengths. On account of the consecutive evaporation of water under light irradiation (about 5 mL reduction of 100 mL in 1 h reaction), the corresponding water was added into the solution. To detect the active species responsible for the degradation of MO, various scavengers, including isopropanol (IPA, 10 mmol/L, $\cdot\text{OH}$ scavenger [36]), N_2 bubbling (100 mL/min, $\cdot\text{O}_2^-$ scavenger [37]), silver nitrate (AgNO_3 , 6 mmol/L, electron scavenger [38]), ammonium oxalate monohydrate ($(\text{NH}_4)_2\text{C}_2\text{O}_4 \cdot \text{H}_2\text{O}$, AO, 1 mmol/L, hole scavenger [39]), KI (1 mmol/L, hole scavenger [40]), disodium ethylenediaminetetraacetate (EDTA-2Na, 1 mmol/L, hole scavenger [41]), and triethanolamine (TEOA, 1 mmol/L, hole scavenger [42]) were employed in the photocatalytic degradation of MO. To observe the mineralization extent of phenol, high performance liquid chromatography (HPLC) and total organic carbon (TOC) measurements were employed. The HPLC tests were performed with

Table 1
Designed sample compositions from different amounts of raw materials.

Sample	$\text{Bi}(\text{NO}_3)_3$ (mol)	TBAB (mol)	Urea (mol)	$\text{Bi}_3\text{O}_4\text{Br}$ (mol)	Bi_2O_3 (mol)	Catalyst composition (wt%)	$\text{Bi}_3\text{O}_4\text{Br}$	Bi_2O_3
Bi_2O_3	0.0051	0	0.0102	0	0.00255	0		100
0.32BB	0.0051	0.0005	0.0017	0.0005	0.0018	31.5		68.5
0.50BB	0.0051	0.0008	0.0017	0.0008	0.00135	49.5		50.5
0.61BB	0.0051	0.0010	0.0017	0.0010	0.00105	61.2		38.8
0.78BB	0.0051	0.0013	0.0017	0.0013	0.0006	78.2		21.8
$\text{Bi}_3\text{O}_4\text{Br}$	0.0051	0.0017	0.0017	0.0017	0	100		0

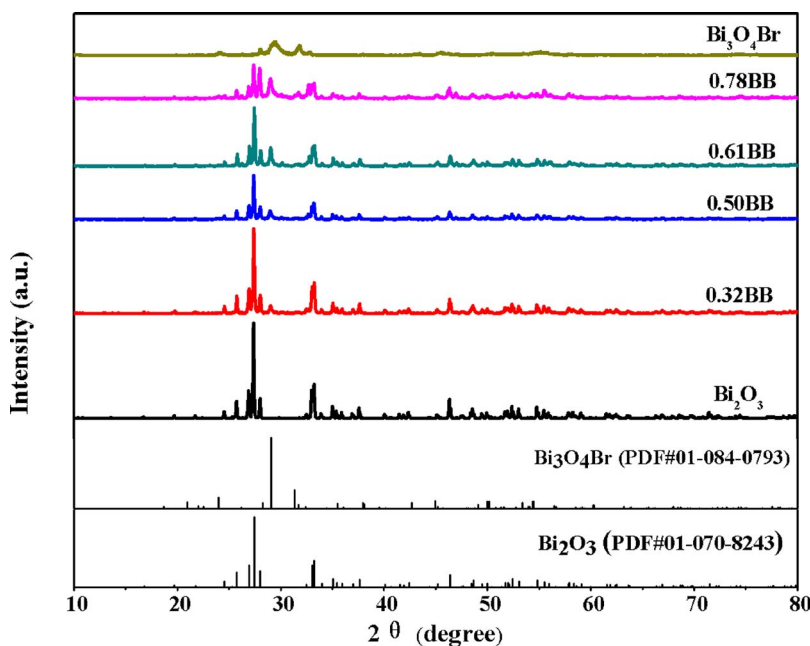


Fig. 1. XRD patterns of α - Bi_2O_3 , $\text{Bi}_3\text{O}_4\text{Br}$ and XBB ($X = 0.32\text{--}0.78$) hybrids.

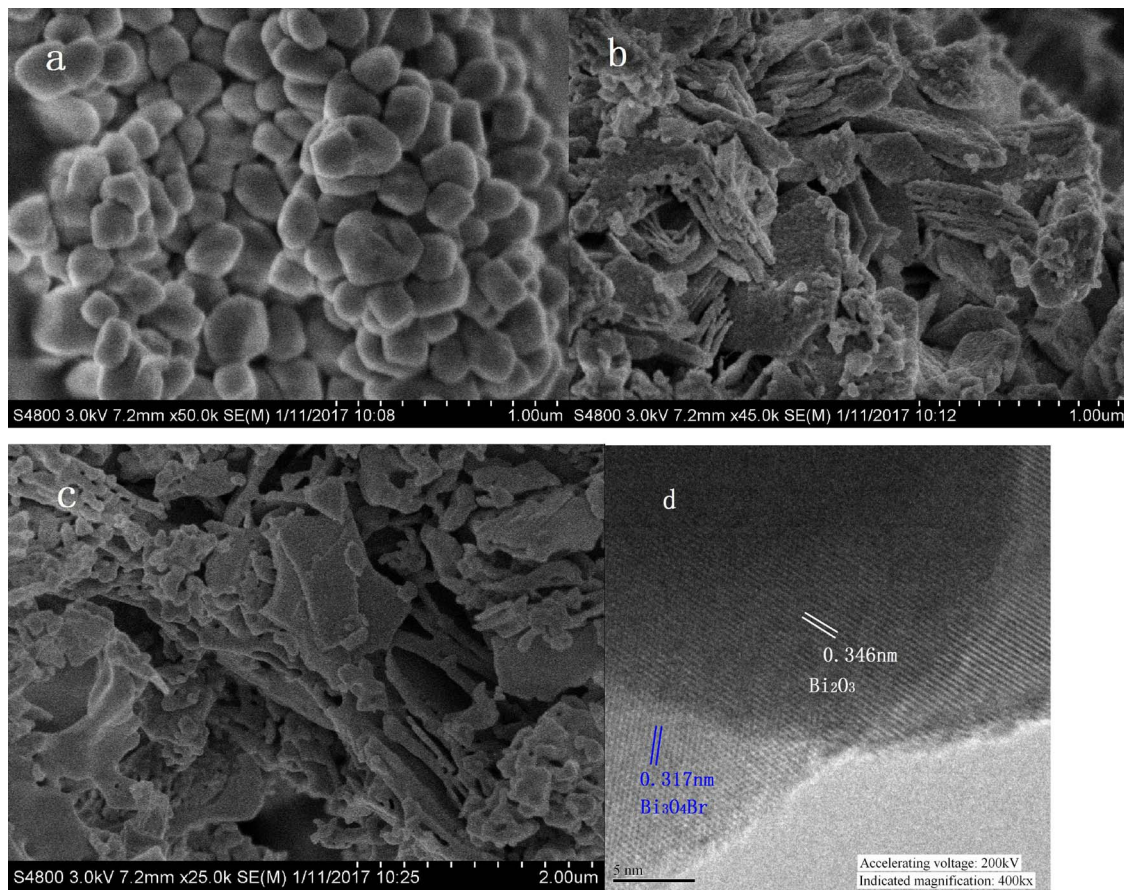


Fig. 2. SEM images of the as-synthesized samples: (a) Bi_2O_3 , (b) $\text{Bi}_3\text{O}_4\text{Br}$, (c) 0.61BB, and (d) HRTEM images of 0.61BB sample.

detection wavelength of 270 nm using a mobile phase mixture of water and methanol in the ratio of 65:35 (v/v) at a flow rate of 1 mL/min. TOC was measured with a Tekmar-Dohrmann Apollo 9000 analyser.

2.4. Photoelectrochemical measurement

Under an applied bias of 0 V, the photocurrent measurements were

carried out on a CHI 660E electrochemical workstation (Shanghai, China) using a standard three electrode quartz cell, which contains a platinum wire as counter electrode, Ag/AgCl (saturated KCl) as reference electrode and a working electrode that was prepared by the photocatalyst films deposited on clean 1.5 cm \times 1.0 cm fluoride-tin oxide (FTO) glass. 0.2 M Na_2SO_4 was used as the electrolyte solution. A 350 W Xe lamp equipped with a 400 nm cut-off filter was taken as the

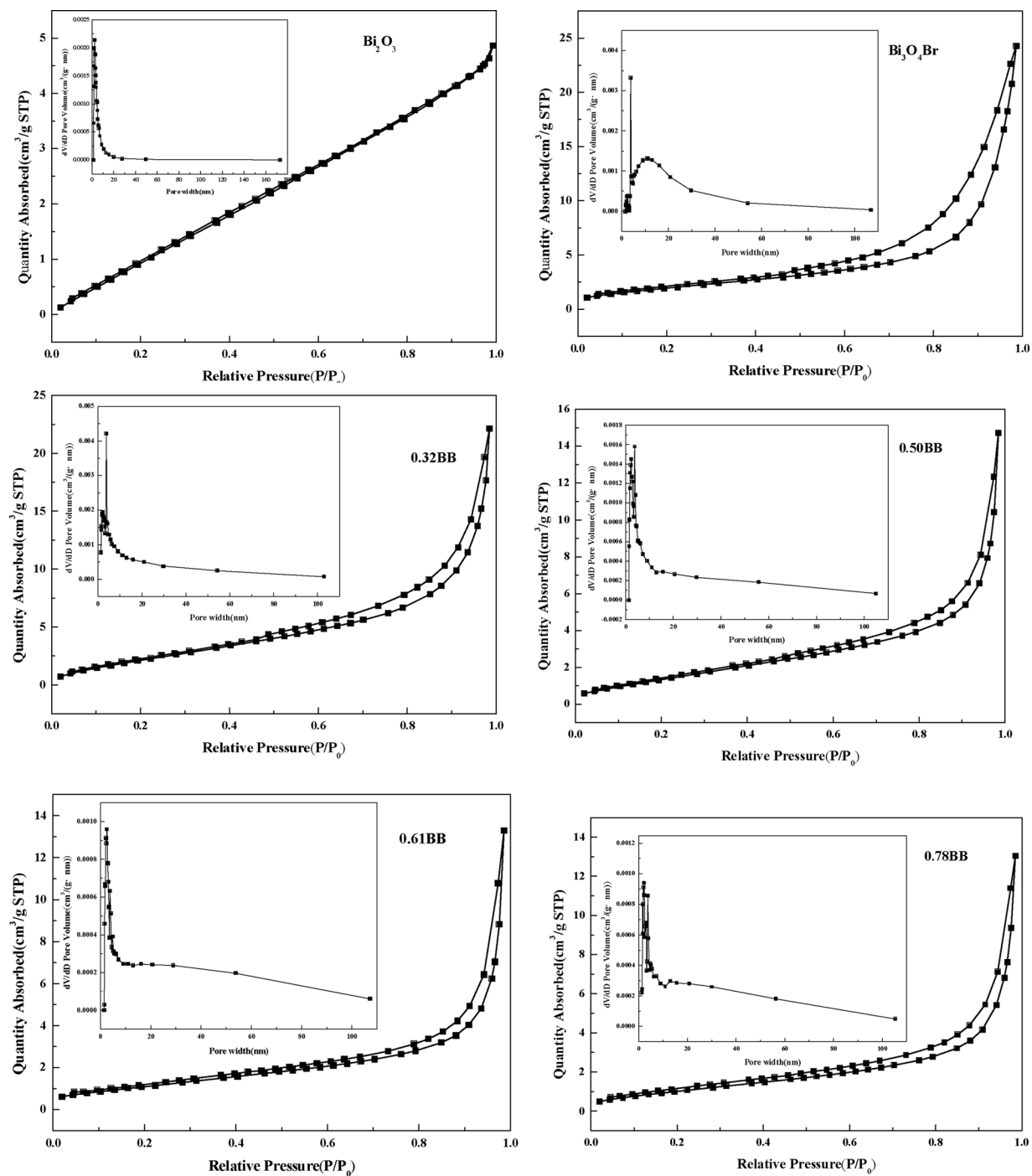


Fig. 3. Nitrogen adsorption-desorption isotherms and the corresponding pore size distribution curve (inset) for the as-synthesized samples.

Table 2
Specific surface areas and pore parameters of the as-prepared samples.

Sample	S_{BET} ($\text{m}^2 \text{g}^{-1}$)	Pore volume ($\text{cm}^3 \text{g}^{-1}$)	Average pore width (nm)
Bi ₂ O ₃	7.703	0.010	2.377
0.32BB	9.837	0.037	3.806
0.50BB	6.044	0.024	3.793
0.61BB	4.355	0.021	2.544
0.78BB	4.172	0.021	2.374
Bi ₃ O ₄ Br	7.588	0.039	3.802

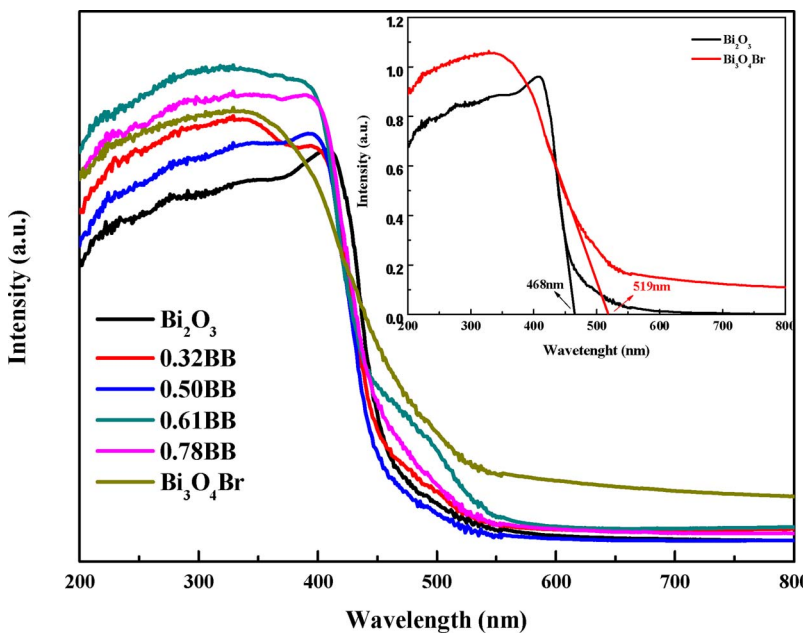
light source. Electrochemical impedance spectroscopy (EIS) was carried out at the open-circuit potential and recorded over a frequency range of $0.1\text{--}1 \times 10^5$ Hz with an ac amplitude of 5 mV.

3. Results and discussion

3.1. Composition, morphology, and structure characterizations

When Bi(NO₃)₃·5H₂O and TBAB were mixed and heated up to about 200 °C, an IL solution was acquired. A potential reaction is proposed as the following Eq. (1):





(1)

To obtain $\text{Bi}_3\text{O}_4\text{Br}$, TBAB is selected not only as assistant fuel but also as the source of bromine. The combustion reaction is proposed as Eq. (2). The formation of Bi_2O_3 is presented as Eq. (3).

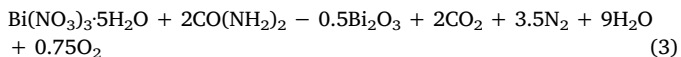
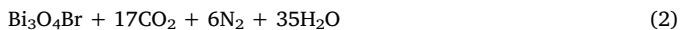


Fig. 1 show the XRD patterns of the as-synthesized samples. The pattern for Bi_2O_3 has a number of peaks that can be well-indexed to α - Bi_2O_3 (PDF#01-070-8243). When TBAB was added and the molar ratio of $\text{Bi}(\text{NO}_3)_3$: TBAB: urea = 3: 1: 1, the sample exhibits a pure $\text{Bi}_3\text{O}_4\text{Br}$ phase (PDF#01-084-0793) and no other crystalline impurities are detected (Because $\text{Bi}_3\text{O}_4\text{Br}$ exhibits weaker diffraction intensity than Bi_2O_3 , it is not obvious to observe the peaks of $\text{Bi}_3\text{O}_4\text{Br}$). Fig. S1 clearly shows the XRD pattern of the as-prepared $\text{Bi}_3\text{O}_4\text{Br}$. When the TBAB amount is less, the samples XBB can be identified as mixed phase of $\text{Bi}_3\text{O}_4\text{Br}$ and Bi_2O_3 . With the decrease of the TBAB amount, the intensities of diffraction peaks of $\text{Bi}_3\text{O}_4\text{Br}$ decrease continuously, while those of Bi_2O_3 increase. This suggests that TBAB plays a key role in adjusting the ratio of $\text{Bi}_3\text{O}_4\text{Br}$ and Bi_2O_3 because it serves as reactant supplying bromine.

The morphology and structure of the as-synthesized samples were observed by SEM and HRTEM images. As presented in Fig. 2a, the sample Bi_2O_3 consists of a large number of regular nanoparticles. The pure $\text{Bi}_3\text{O}_4\text{Br}$ sample shown in Fig. 2b exhibits mainly a hierarchical and sheets morphology, revealing its layer structure. Fig. 2c shows SEM images of the resulting 0.61BB hybrid, in which the Bi_2O_3 spheres are uniformly adhered to the surface of $\text{Bi}_3\text{O}_4\text{Br}$ nanosheets, indicating their co-existence in the sample. In order to analyze the interface between the two phases in the composites, the HRTEM image of 0.61BB composite is given in Fig. 2d. It can be seen that clear lattice fringes of $\text{Bi}_3\text{O}_4\text{Br}$ and Bi_2O_3 can be observed. The largest portion with 0.317 nm lattice fringe was ascribed to (114) plane of $\text{Bi}_3\text{O}_4\text{Br}$ and the 0.346 nm lattice fringe is ascribed to the (002) plane of Bi_2O_3 , which further implies the formation of heterojunction structure.

Fig. 3 presents the nitrogen absorption-desorption isotherms and the corresponding BJH pore size distribution curves (insets) of the as-synthesized samples. According to the IUPAC classifications, all isotherms

Fig. 4. UV-vis diffuse reflectance spectra of the as-prepared samples; the inset displays λ_g of $\text{Bi}_3\text{O}_4\text{Br}$ and Bi_2O_3 .

are identified as type IV with H3 hysteresis loop [43]. Especially all the samples containing $\text{Bi}_3\text{O}_4\text{Br}$ show obvious pore features while pure Bi_2O_3 does not, which are consistent with their SEM results. The calculated BET specific surface areas (S_{BET}) and the pore parameters of all the samples are listed in Table 2. It can be seen that there is only small difference in S_{BET} of the samples, S_{BET} should not play the decisive role for MO adsorption and degradation.

3.2. Optical characteristic and energy band structure

The optical properties of the as-prepared samples were characterized by UV-vis DRS, as shown in Fig. 4. It is seen that all the samples exhibit strong absorption in the visible light region up to around 500 nm. Compared to pure Bi_2O_3 and $\text{Bi}_3\text{O}_4\text{Br}$, 0.61BB and 0.78 hybrids display stronger photo-absorption from 200 nm to 420 nm; meanwhile, it can be also seen that there is no regularity in the light absorption of different ratios of $\text{Bi}_3\text{O}_4\text{Br}/\text{Bi}_2\text{O}_3$ samples, which implies there is light interaction between the counterparts. The energy band gaps (E_g) of Bi_2O_3 and $\text{Bi}_3\text{O}_4\text{Br}$ are estimated to be 2.65 eV and 2.39 eV based on the empirical equation $E_g = 1240/\lambda_g$ (nm) respectively [44], where λ_g is the threshold wavelength value that is obtained from the crossing point of the horizontal axis and tangent parts of the spectrum as shown in the inset of Fig. 4.

In order to deeply elucidate the energy band structures of Bi_2O_3 and $\text{Bi}_3\text{O}_4\text{Br}$, the Mott-Schottky experiments were carried out and the results are shown in Fig. 5a. The positive slope of the C^{-2} -E plot suggests that both Bi_2O_3 and $\text{Bi}_3\text{O}_4\text{Br}$ belong to n-type semiconductors [45]. The flat band potential (V_{fb}) obtained by the cross point of X axis with the tangent line of linear potential curves is approximately -1.15 V and -1.22 V vs Ag/AgCl for Bi_2O_3 and $\text{Bi}_3\text{O}_4\text{Br}$, respectively. Using the following conversion formula (4) [46–48]: $E_{\text{RHE}} = E_{\text{Ag/AgCl}} + 0.059 \text{ pH} + E_{\text{Ag/AgCl}}^0$ ($E_{\text{Ag/AgCl}}^0 = +0.199$ V, and pH = 6.8 in this research) (4), the V_{fb} can be calculated to be -0.55 V and -0.62 V vs. RHE (reversible hydrogen electrode), respectively. RHE corresponds to the normal hydrogen electrode (NHE) at pH = 0. Furthermore, V_{fb} of n-type semiconductors is very close to the bottom of CB potential (E_{CB}) [49], thus the E_{CB} values of Bi_2O_3 and $\text{Bi}_3\text{O}_4\text{Br}$ are -0.55 V and -0.62 V vs NHE, respectively. The valence band top potential (E_{VB}) can be obtained using Eq. (4) [50]:

$$E_{\text{CB}} = E_{\text{VB}} - E_g \quad (4)$$

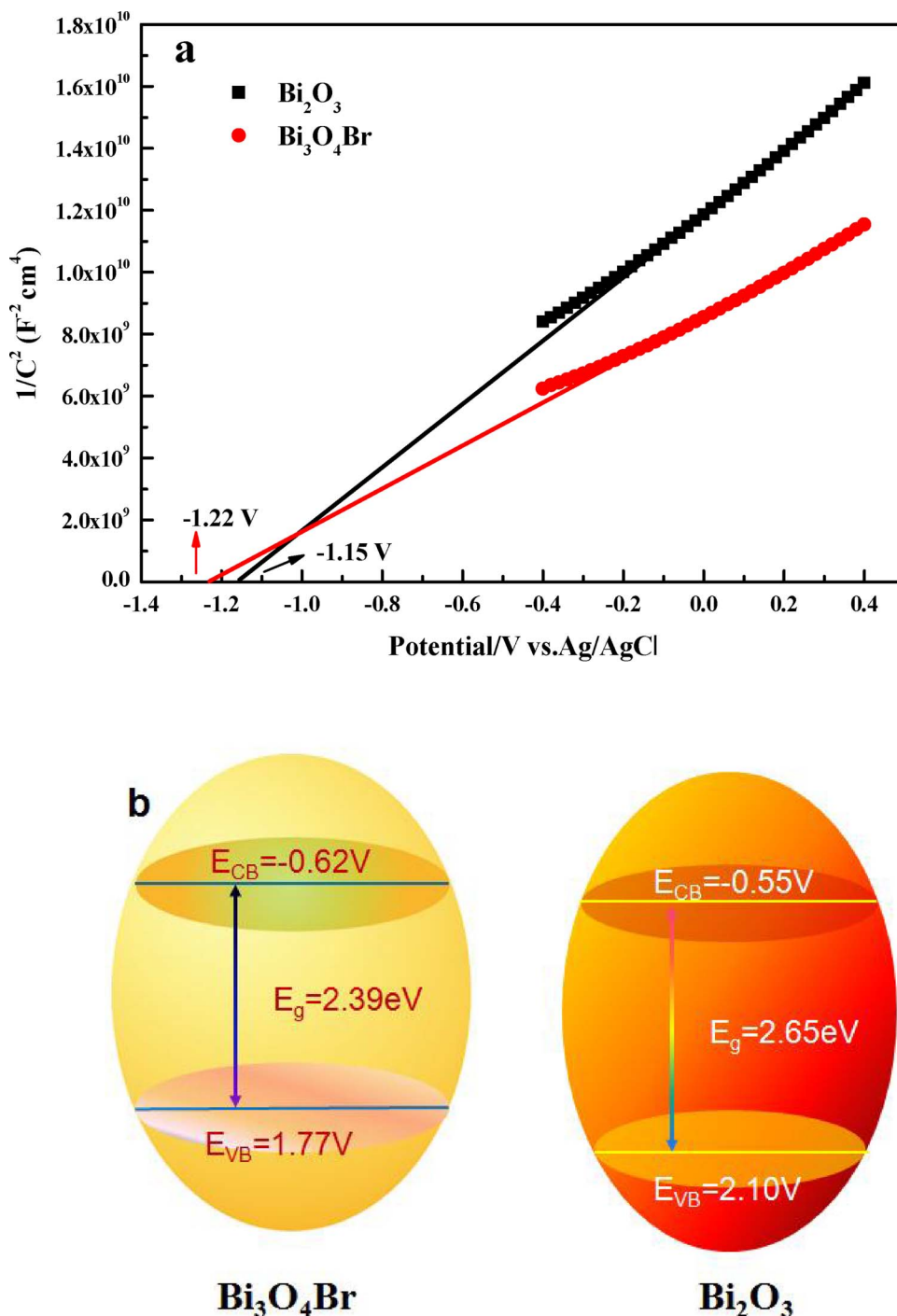


Fig. 5. (a) Mott-Schottky plots of Bi_2O_3 and $\text{Bi}_3\text{O}_4\text{Br}$, and (b) the proposed energy band potentials of Bi_2O_3 and $\text{Bi}_3\text{O}_4\text{Br}$.

E_g of Bi_2O_3 and $\text{Bi}_3\text{O}_4\text{Br}$ is 2.65 and 2.39 eV respectively, consequently the E_{VB} value of the as-prepared Bi_2O_3 and $\text{Bi}_3\text{O}_4\text{Br}$ is estimated to be 2.10 and 1.77 V vs. NHE, respectively. Based on the above experimental values, the energy band structure of Bi_2O_3 and $\text{Bi}_3\text{O}_4\text{Br}$ is shown in Fig. 5b.

3.3. Chemical interaction test by XPS

To further verify the formation of heterojunction, XPS spectra of the samples were characterized. Fig. 6a shows the XPS survey spectra of Bi_2O_3 , $\text{Bi}_3\text{O}_4\text{Br}$ and 0.61BB hybrid. The C signal in the survey scan spectra comes from adventitious carbon [51]. Only Bi and O signals were detected in the XPS spectra of pure Bi_2O_3 . The spectra of $\text{Bi}_3\text{O}_4\text{Br}$

and 0.61BB hybrid samples consist of the Bi, O and Br elements without detecting existence of other impurity element. It can be observed that the Br peak intensity of the 0.61BB hybrid is significantly lower than that of pure $\text{Bi}_3\text{O}_4\text{Br}$, which indicates that the 0.61BB hybrid contains a small amount of $\text{Bi}_3\text{O}_4\text{Br}$. As shown in Fig. 6b, the high-resolution spectra of Br3d are accurately deconvoluted into two peaks corresponding to Br3d and 3d5/2 at binding energies (BE) around 69.11 and 68.05 eV, respectively [52]. However, the peaks in the 0.61BB sample are observed at 68.87 and 68.02 eV, which are lower than those for pure $\text{Bi}_3\text{O}_4\text{Br}$. Such shifts can be attributed to the chemical interaction between Bi_2O_3 and $\text{Bi}_3\text{O}_4\text{Br}$, instead of a simple physical connect.

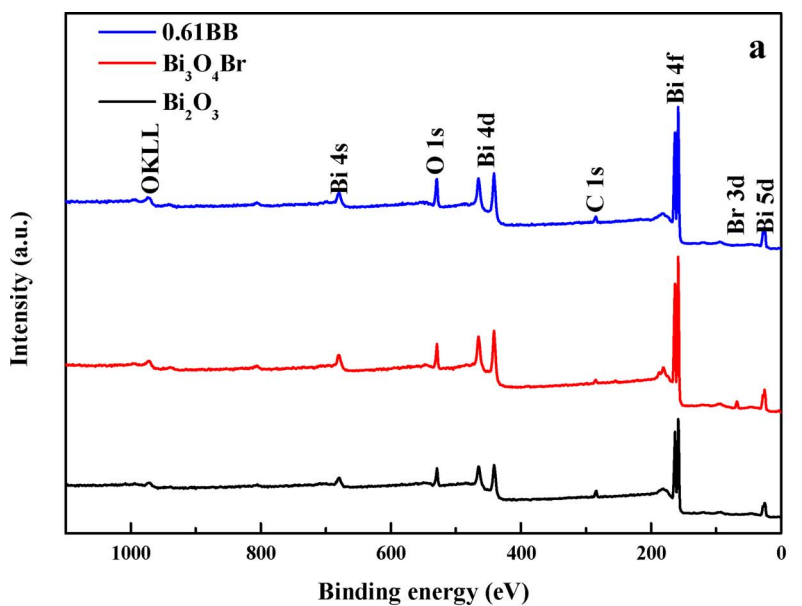
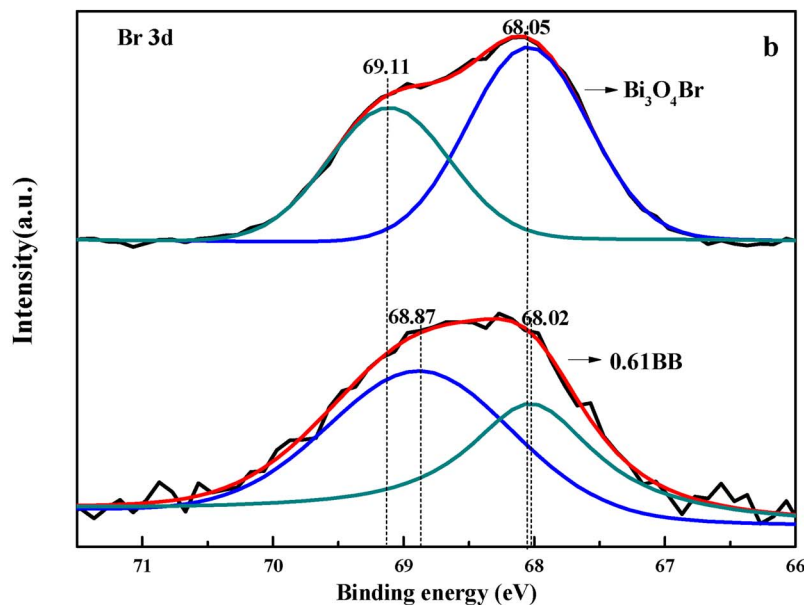


Fig. 6. (a) XPS survey spectra of Bi_2O_3 , $\text{Bi}_3\text{O}_4\text{Br}$ and 0.61BB samples, (b) High-resolution XPS spectra of $\text{Bi}_3\text{O}_4\text{Br}$ and 0.61BB samples in the regions of $\text{Br}3\text{d}$.



3.4. Photocatalytic activity

To explore the photocatalytic performance of the resultant samples in practical application, the photocatalytic degradation of dye molecules (MO) and colorless organic pollutant (phenol) over the as-synthesized samples was evaluated under visible light irradiation, as shown in Fig. 7. Under the same test conditions, the degradation efficiency of 10 mg/L of MO and 50 mg/L phenol are only 1% in the absence of the photocatalyst, indicating that the self-photolysis of MO and phenol can be negligible. When as-prepared photocatalysts were introduced to the MO degradation system, only 28.0% and 48.0% degradation yield in 100 min occurred relative to Bi_2O_3 and $\text{Bi}_3\text{O}_4\text{Br}$, respectively, while all of the synthesized composites (sample XBB) exhibit enhanced photocatalytic activities. Especially a 98.0% removal can be obtained over sample 0.61BB, indicating its excellent visible light photocatalytic performance. The photocatalytic degradation kinetics of MO with low initial concentration is evaluated by the reaction rate constant listed in the following the pseudo-first-order kinetics equation [40]:

$$\ln C_0/C_t = kt + \ln C_0/C_1 \quad (6)$$

where C_0 is the initial concentration of MO (10 mg/L), C_1 and C_t are the concentration after adsorption and the reactant concentrations at reaction time t , respectively, and k (min^{-1}) is the apparent reaction rate constant. In treating the photocatalytic data for fitting, the intercept on the y-axis is coerced at the value of $\ln(C_0/C_1)$ of each sample. The results (Fig. 7c) show that the sample 0.61BB exhibits the highest photocatalytic ability among these samples. The k value (0.03703 min^{-1}) of heterojunction 0.61BB is approximately 11.6 and 5.2 times that of the single Bi_2O_3 (0.0032 min^{-1}) and $\text{Bi}_3\text{O}_4\text{Br}$ (0.00716 min^{-1}), respectively. Meanwhile, all the fitted correlation coefficients (R) are above 0.9889.

In order to exclude the photosensitization of colored organic dyes, the colorless phenol was selected as objective pollutant, which gives the same results (as shown in Fig. 7b and 7d). The composites show a higher photocatalytic performance compared with pure Bi_2O_3 and

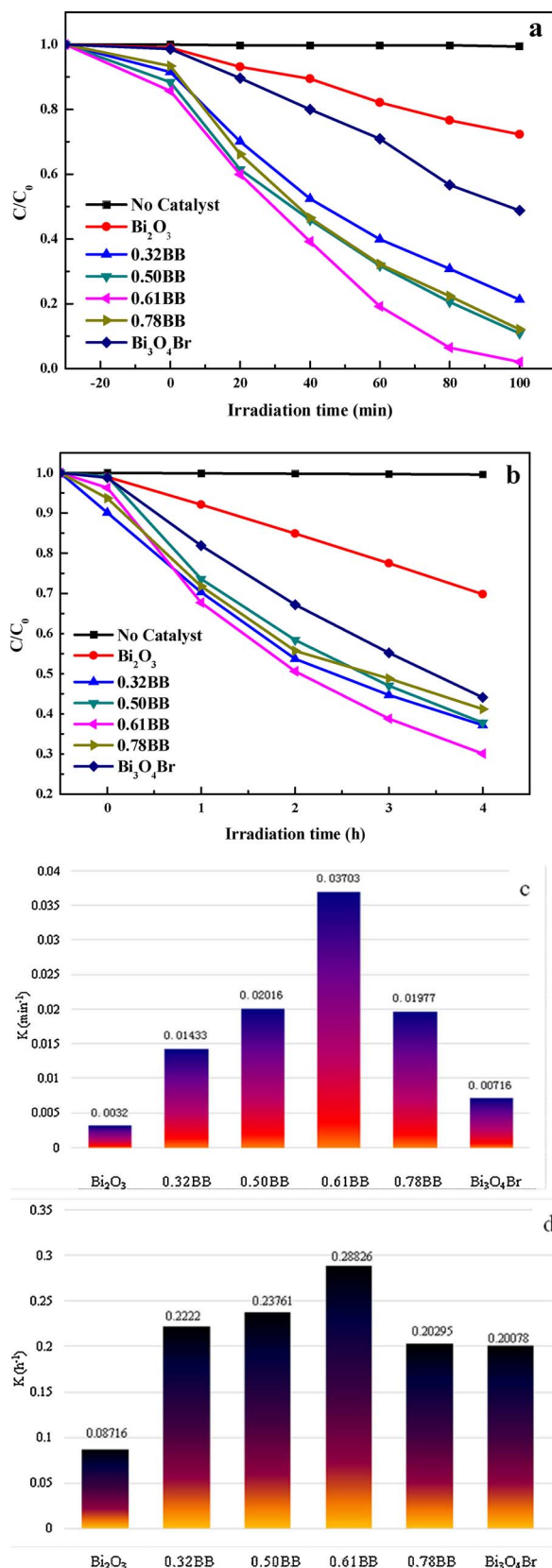


Fig. 7. Time-course variation of C/C_0 of (a) 10 mg L^{-1} of MO, (b) 50 mg L^{-1} of phenol under visible light illumination over various catalysts, and (c), (d) the corresponding reaction rate constants (k) for MO and phenol, respectively. (pollutant volume = 100 mL , catalyst amount = 100 mg).

$\text{Bi}_3\text{O}_4\text{Br}$ 0.61BB hybrid reaches 70% degradation rate for phenol in 4 h with a reaction rate constant 3.3 and 1.4 times that of Bi_2O_3 and $\text{Bi}_3\text{O}_4\text{Br}$, respectively. The above results indicate that all the composites have higher photocatalytic activities than pristine Bi_2O_3 and $\text{Bi}_3\text{O}_4\text{Br}$.

The HPLC chromatogram of phenol aqueous solution over 0.61BB at different times are shown in Fig. S2. It is seen that almost no other obvious peaks can be detected except for some tiny peaks at retention times of 1.137, 1.477, and 5.110 min, implying that phenol can be mineralized directly to CO_2 and H_2O . Meanwhile, TOC removal of phenol in 4 h is 65.2%, slightly lower than the degradation yield (69.9%) measured by spectrophotometer, which also implies that mineralization is completed.

3.5. Separation efficiency measurement of charge carriers

To understand the improvement of photocatalytic activities for the heterojunction materials, we further studied the transient photocurrent responses and EIS. Fig. 8a shows the transient photocurrent curves of pure Bi_2O_3 , $\text{Bi}_3\text{O}_4\text{Br}$ and the XBB composites for each switch-on and – off event in intermittent 30 s on-off cycles under simulated solar light irradiation. It is worth noting that no obvious photocurrent intensities of the whole samples are reduced, even after six intermittent on-off cycles, which show they possess excellent reproducibility and stability. Unexpectedly, it is clear that the photocurrent density of the 0.61BB hybrid electrode is lower than that of pure $\text{Bi}_3\text{O}_4\text{Br}$, while the intensity from $\text{Bi}_3\text{O}_4\text{Br}$ electrode is the highest. This result implies that layer structured $\text{Bi}_3\text{O}_4\text{Br}$ has the highest separation efficiency of photo-induced charges and the introduction of sphere like Bi_2O_3 would reduce the separation of charge carriers. Therefore, not all the heterojunctions would surely result in the enhanced carriers transfer.

To avoid the influence of some accidental factors on the photocurrent measurements, the EIS tests were performed to further investigate the resistance of interfacial charge transfer process. A smaller arc radius of EIS Nyquist plot means a lower resistance of electron transfer and an effective separation of photo-generated electron-hole pairs [53]. Same interesting finding is seen from Fig. 8b that the arc radius of the pure $\text{Bi}_3\text{O}_4\text{Br}$ is the smallest among these semiconductors, really indicating that the $\text{Bi}_3\text{O}_4\text{Br}$ owns a more effective separation of photo-generated electron-hole pairs than heterojunctions.

To further verify this abnormal phenomenon, the photophysical characteristics of charge carriers is investigated by time-resolved photoluminescence decay technique. Fig. 9 shows the decay curves of Bi_2O_3 , $\text{Bi}_3\text{O}_4\text{Br}$ and 0.61BB, which are fitted and the corresponding lifetimes and percentages are listed in Table 3. It is seen that $\text{Bi}_3\text{O}_4\text{Br}$ has the longest lifetime, meaning its highest separation efficiency of electrons and holes.

Nevertheless, in theory, higher separation efficiency always leads to faster degradation rate, while these photoelectrochemical test results are not consistent with the observed photocatalytic activity. Hence it is deduced that the enhanced photocatalytic activities of heterostructured composites cannot be attributed to the separation efficiency of charge carriers. There are other more important reasons responsible for the improved photocatalytic performance of heterojunctions.

3.6. Active species detection

In order to deeply investigate the reaction mechanism during the photocatalytic process, the photocatalytic degradation of MO over pure $\text{Bi}_3\text{O}_4\text{Br}$ and 0.61BB hybrid were further explored through a battery of control experiments. As shown in Fig. 10a, after adding IPA ($\cdot\text{OH}$ scavenger) and bubbling N_2 (to remove oxygen that was dissolved in the solution) into the $\text{Bi}_3\text{O}_4\text{Br}$ system, the photodegradation efficiency kept nearly unchanged relative to without scavenger. However, with addition of ammonium oxalate monohydrate (AO, hole scavenger), the MO removal was significantly depressed, suggesting that the critical degradation process is via direct photogenerated hole oxidation. As can

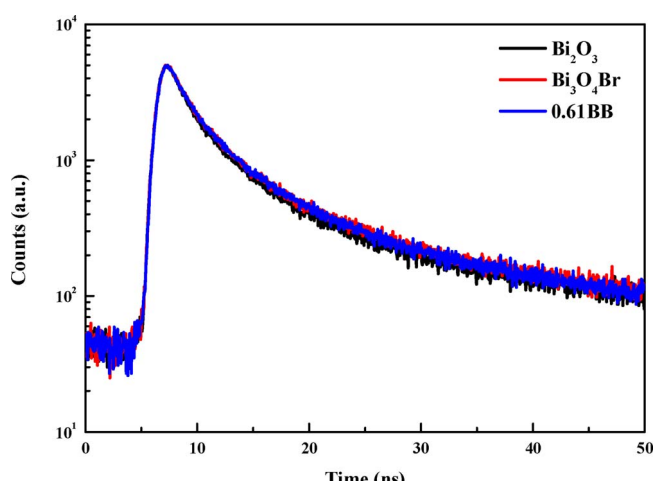
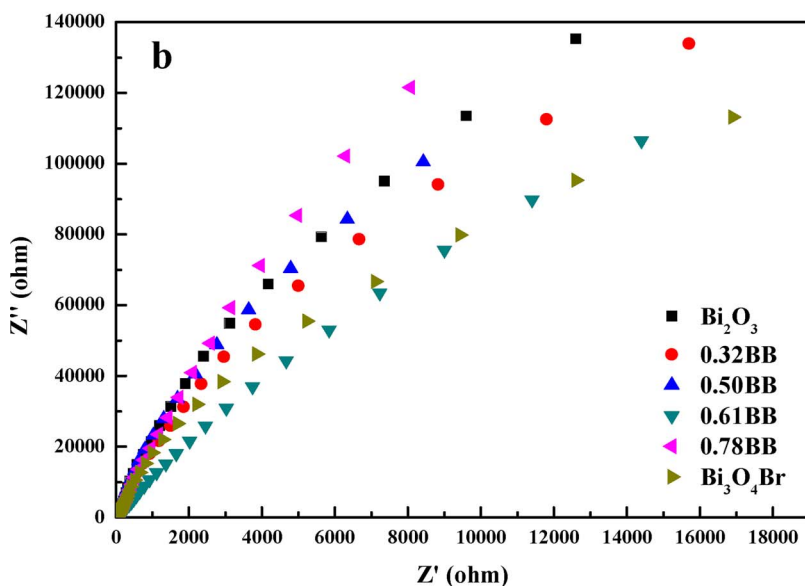
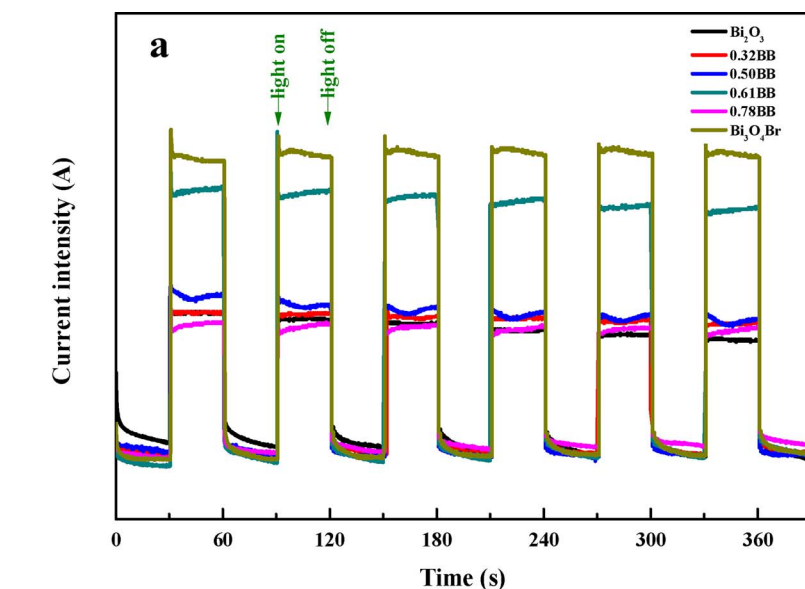


Fig. 9. Time-resolved fluorescence decay spectra of Bi_2O_3 , $\text{Bi}_3\text{O}_4\text{Br}$ and 0.61BB hybrid.

Table 3

The fitted lifetimes and the corresponding percentages of Bi_2O_3 , $\text{Bi}_3\text{O}_4\text{Br}$ and 0.61BB hybrid.

Sample	τ_1 (ns)	P1(%)	τ_2 (ns)	P2(%)	τ_3 (ns)	P3(%)
Bi_2O_3	1.37	26.18	4.77	43.19	22.86	30.63
$\text{Bi}_3\text{O}_4\text{Br}$	1.62	28.07	5.53	40.67	26.15	31.25
0.61BB	1.52	26.34	5.31	42.93	23.71	30.73

be seen from Fig. 10b, the photocatalytic degradation of MO on 0.61BB composite is almost not affected by adding IPA. When N_2 was added into the system, there is a decline in the removal yields of MO to some extent, illustrating that $\cdot\text{O}_2^-$ exerts certain influence on the degradation of MO and it is also a kind of reactive species. After adding AO, the inhibitory photocatalytic degradation of MO is observed more apparently in comparison with $\text{Bi}_3\text{O}_4\text{Br}$ system, indicating that the hole oxidation ability of heterojunction is enhanced. Moreover, the photocatalytic degradation is noticeably increased in the presence of silver nitrate (AgNO_3 , e^- scavenger), indirectly indicating that the photo-generated holes are increased due to the capture of electrons and play a

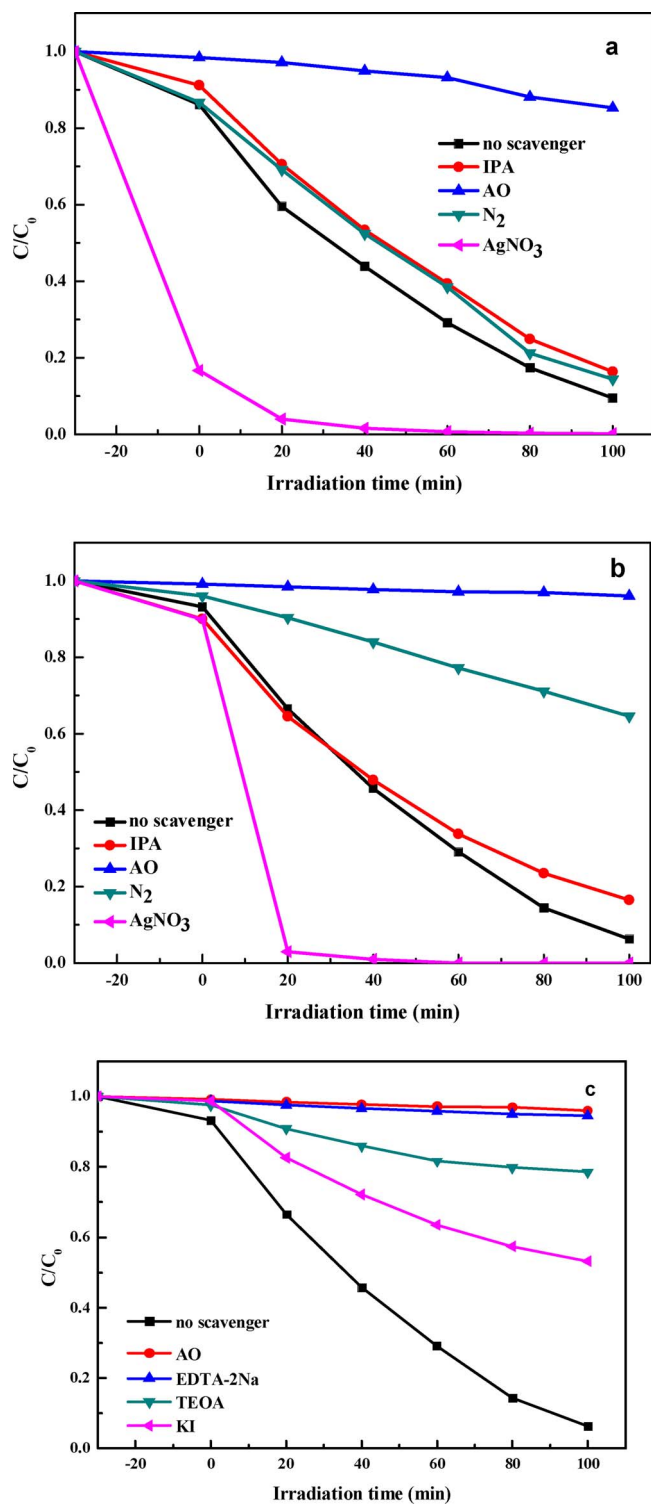


Fig. 10. Control experiments of the photodegradation of MO over (a) $\text{Bi}_3\text{O}_4\text{Br}$, (b) 0.61BB hybrid in the presence of various radical scavengers, and (c) 0.61BB hybrid in the presence of various hole scavengers. ($[\text{MO}] = 10 \text{ mg L}^{-1}$, MO volume = 100 mL, catalyst amount = 100 mg).

major role in photocatalytic degradation MO. To further confirm the role of hole in degradation of MO, various hole scavengers including EDTA-2Na, TEOA, and KI were employed. The results shown in Fig. 10c clearly indicate that all the scavengers have decreased the degradation efficiency of MO.

Fig. 11a shows the time course of the conversion percentage of *p*-nitro blue tetrazolium chloride (NBT, $2.5 \times 10^{-5} \text{ mol/L}$) over Bi_2O_3 ,

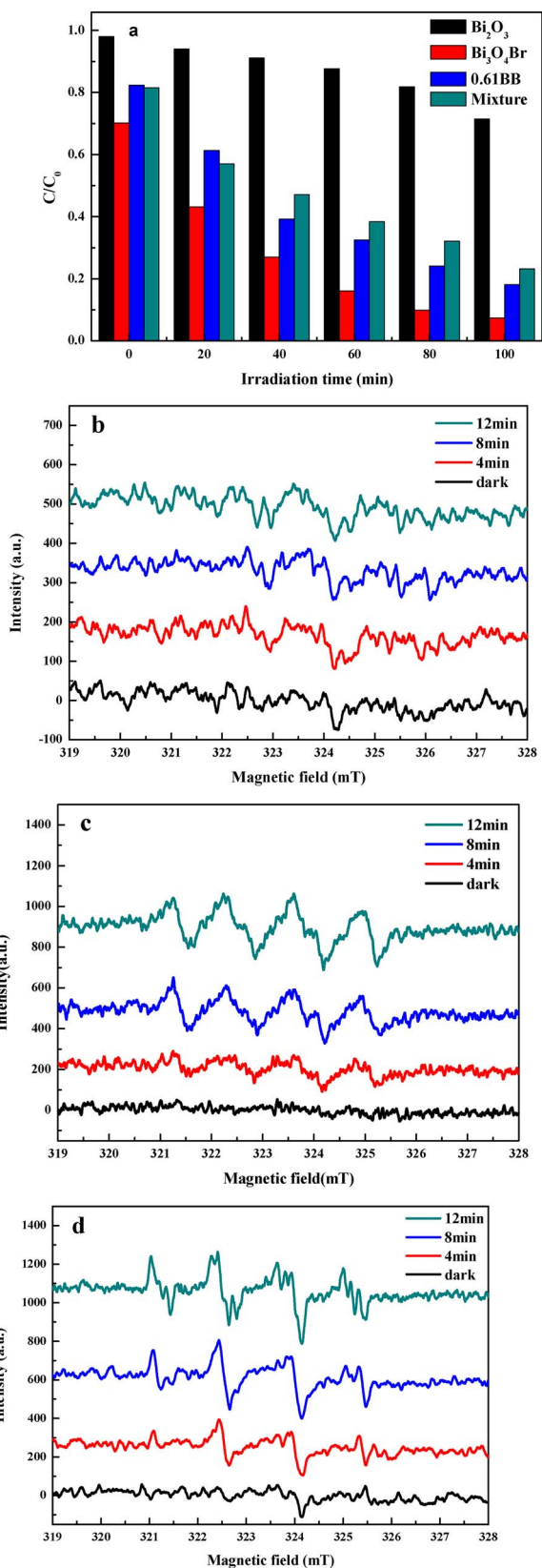


Fig. 11. (a) Time course of conversion percentage of NBT concentration over Bi_2O_3 , $\text{Bi}_3\text{O}_4\text{Br}$, 0.61BB hybrid and mechanical mixture of Bi_2O_3 and $\text{Bi}_3\text{O}_4\text{Br}$; ESR spectra of DMPO- O_2^- adducts over (b) Bi_2O_3 , (c) $\text{Bi}_3\text{O}_4\text{Br}$, and (d) 0.61BB hybrid in the dark and after irradiation at various times.

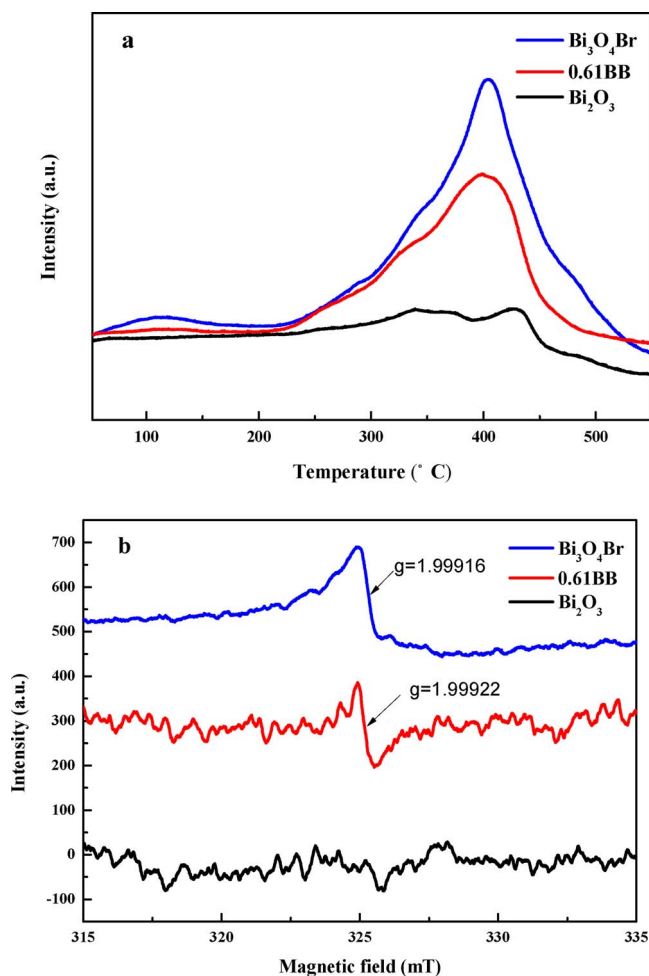


Fig. 12. (a) O₂-TPD spectra of Bi₂O₃, Bi₃O₄Br, and 0.61BB hybrid; (b) EPR signals of Bi₂O₃, Bi₃O₄Br, and 0.61BB samples for surface oxygen vacancies.

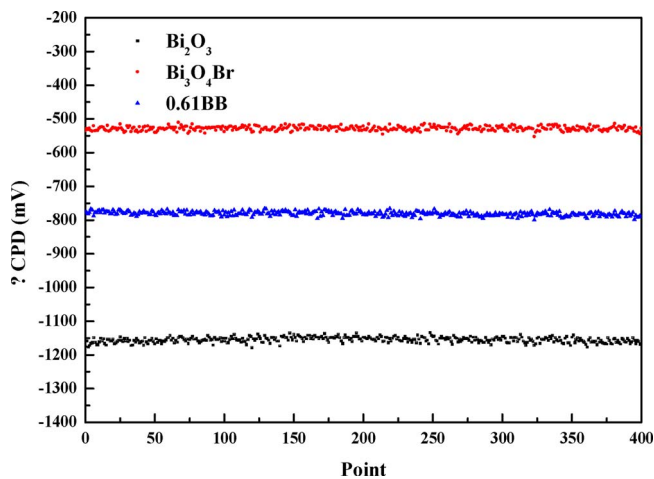


Fig. 13. Work function mapping of Bi₂O₃, Bi₃O₄Br and 0.61BB hybrid measured by Kelvin probe in air.

Bi₃O₄Br, 0.61BB hybrid and their according mechanical mixture sample (0.061 g Bi₃O₄Br and 0.039 g Bi₂O₃) respectively. $\cdot\text{O}_2^-$ radicals can react with NBT that has a maximum absorption wavelength at 260 nm, while the product of $\cdot\text{O}_2^-$ and NBT does not [54,55]. Therefore, the peak reduction of NBT can represent the amount $\cdot\text{O}_2^-$ radicals. It is clear that the Bi₃O₄Br exhibits the highest degradation ability for NBT, indicating it's the most powerful ability for activating O₂ to generate $\cdot\text{O}_2^-$.

Compared with mechanical mixture sample, the generation $\cdot\text{O}_2^-$ of 0.61BB hybrid is enhanced, which can be ascribed to the interaction between Bi₂O₃ and Bi₃O₄Br. Meanwhile, there is very little decrease of NBT concentration over pure Bi₂O₃, implying its poor ability to activate molecular oxygen.

To further directly confirm the generation of $\cdot\text{O}_2^-$ radicals in the photocatalytic process, the ESR technique was employed based on the fact that $\cdot\text{O}_2^-$ can be trapped by 5,5-dimethyl-*l*-pyrroline-N-oxide (DMPO) [56]. From Fig. 11b, it is found that there is almost no DMPO- $\cdot\text{O}_2^-$ signal over pure Bi₂O₃ under visible light irradiation, which is accordance with the NBT degradation result. As shown in Fig. 11c-d, the characteristic peaks of DMPO- $\cdot\text{O}_2^-$ adducts are detected over both Bi₃O₄Br and 0.61BB hybrid. In addition, there is steady intensity increase of $\cdot\text{O}_2^-$ radicals in both Bi₃O₄Br and 0.61BB hybrid with the time increase, which indicates that $\cdot\text{O}_2^-$ radicals are gradually increased under light irradiation.

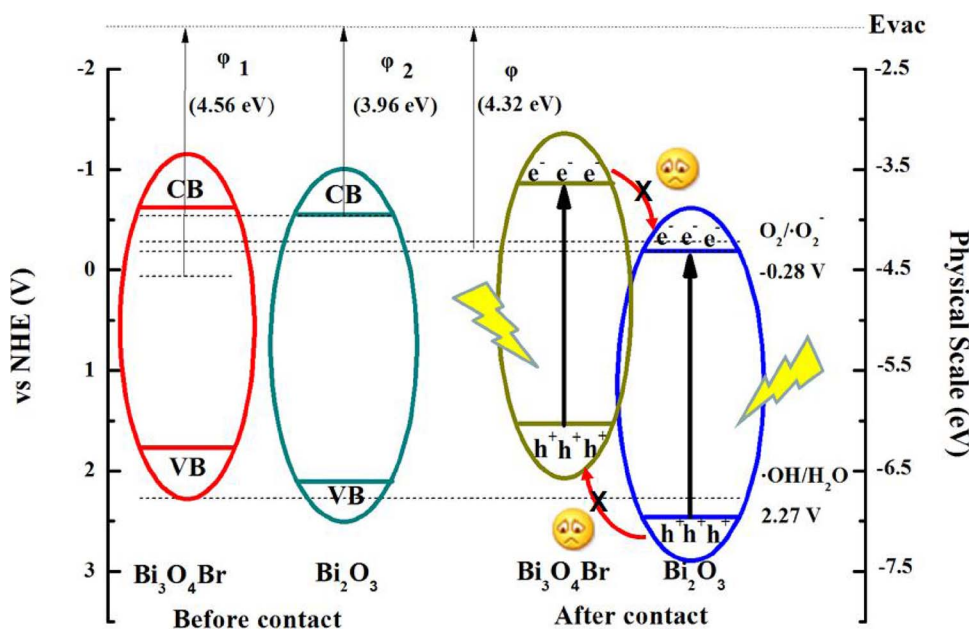
To study the reason why Bi₃O₄Br has so much higher $\cdot\text{O}_2^-$ generation ability than Bi₂O₃, O₂-TPD test was taken which can directly exhibit the O₂ desorption behavior on the surface of photocatalysts. Generally speaking, the signals recorded below 700 °C can be attributed to the α -O₂ desorption and originated from the oxygen species adsorbed on the surface [57]. O₂-TPD spectra of Bi₂O₃, Bi₃O₄Br, and 0.61BB samples are shown in Fig. 12a. It is clear that the desorption peak of O₂ from Bi₃O₄Br surface is the most intense one, indicating that Bi₃O₄Br can adsorb more O₂ than Bi₂O₃ and 0.61BB hybrid. Meanwhile, the desorption peak intensity of Bi₂O₃ is very weak, exhibiting its poor ability to adsorb O₂. To further detect whether surface oxygen vacancy is the factor affecting O₂ adsorption, ESR spectra are shown in Fig. 12b. It is seen that there is a clear ESR signal for sample Bi₃O₄Br at $g = 1.99916$, which is ascribed to the superoxide ion that is derived from the atmospheric oxygen adsorbed on the surface oxygen vacancy of Bi₃O₄Br [58]. On the contrary, no obvious peak can be observed for Bi₂O₃ and there is a signal with medium intensity over sample 0.61BB. The difference of oxygen vacancy in Bi₃O₄Br and Bi₂O₃ may be related to their structure. As a layer-type matter, the oxygen atoms of Bi₃O₄Br are highly exposed and can easily release to the atmosphere, leaving oxygen vacancies. The result indicates the surface oxygen vacancy may be one of the factors in charge of O₂ adsorption on photocatalysts. When the conduction band potential of a photocatalyst is more negative than the standard redox potential of O₂/ $\cdot\text{O}_2^-$ (E^0 (O₂/ $\cdot\text{O}_2^-$) = -0.28 V vs. NHE) [26], the higher adsorption amounts of O₂, the more $\cdot\text{O}_2^-$ radicals produce, which conforms to the NBT and ESR of DMPO- $\cdot\text{O}_2^-$ results.

3.7. Photocatalytic mechanism

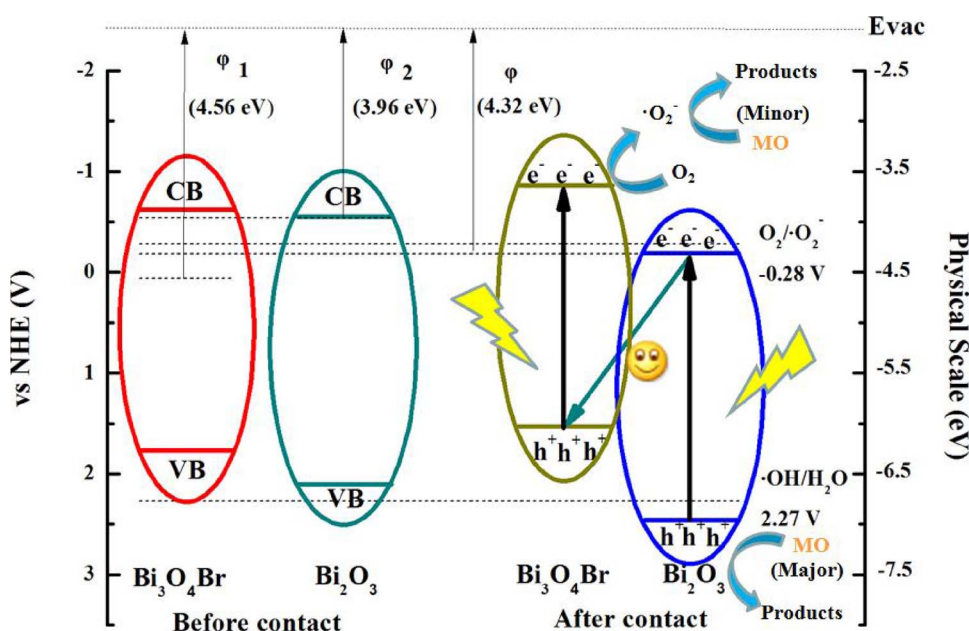
Work functions (φ) of the Bi₂O₃, Bi₃O₄Br and 0.61BB films are measured by Kelvin probe, which directly provides the contact potential differences (CPDs) between the samples and the Au probe [59]. Fig. 13 shows the work function mapping results of loaded on ITO glass. The φ values are calculated by using the following equation:

$$\varphi_{\text{sample}} = \varphi_{\text{Au}} + e\text{CPD}, (\varphi_{\text{Au}} = 5.1 \text{ eV}) \quad (7)$$

Therefore, the working function values of the Bi₂O₃, Bi₃O₄Br and 0.61BB films are about 3.96 eV, 4.56 eV, and 4.32 eV, respectively. These data imply that the Fermi level of 0.61BB is between those of the two semiconductors. On the basis of the experimental results and the φ values, a theoretical transfer process of the photo-generated charges mechanism of 0.61BB composite is proposed, as shown in Scheme 1. When Bi₃O₄Br and Bi₂O₃ are combined to form heterojunction, the Fermi level of Bi₂O₃ moves down, while that of Bi₃O₄Br moves up until the equilibrium state is formed [60]. In line with the movement of the Fermi level, the whole energy band of Bi₃O₄Br is raised up, meanwhile that of Bi₂O₃ is lowered. Upon visible light irradiation ($\lambda > 400$ nm), both Bi₃O₄Br and Bi₂O₃ can be activated, generating the photo-induced



Scheme 1. Energy band structure and impossible transfer route of the photo-generated carriers over hybrid.



Scheme 2. Energy band diagram and the proposed potential photocatalytic mechanism of the hybrid under visible light irradiation.

electrons and holes. If the electrons on the CB of $\text{Bi}_3\text{O}_4\text{Br}$ flow to the CB of Bi_2O_3 and holes on the VB of Bi_2O_3 transfer to the VB of $\text{Bi}_3\text{O}_4\text{Br}$, the electrons on CB of Bi_2O_3 at this position (redox potential of -0.19 V) cannot react with the O_2 to form $\cdot\text{O}_2^-$ radicals ($E^0(\text{O}_2/\cdot\text{O}_2^-) = -0.28\text{ eV}$ vs. NHE), and with the rise up of holes position, the direct oxidation ability of holes on $\text{Bi}_3\text{O}_4\text{Br}$ would be decreased. As a result, the photocatalytic activity should become worse, which is opposed to the degradation results of MO and phenol. Hence, the proposed **Scheme 1** for photo-induced carriers transfer route is impossible.

On the basis of the above analysis, a reasonable energy band diagram of $\text{Bi}_3\text{O}_4\text{Br}/\text{Bi}_2\text{O}_3$ composite and the corresponding z-scheme photocatalytic mechanism is proposed in **Scheme 2**. Under visible light irradiation, the photo-induced electrons of Bi_2O_3 transfer to combine with the holes on $\text{Bi}_3\text{O}_4\text{Br}$, leaving more holes on Bi_2O_3 engaging in the oxidation reaction of pollutants. Because the formation of heterojunction lowers the position of holes on Bi_2O_3 , their ability as oxidants is strengthened greatly [61,62], resulting in the higher photocatalytic activity.

4. Conclusions

$\text{Bi}_3\text{O}_4\text{Br}/\alpha\text{-Bi}_2\text{O}_3$ heterojunctions are prepared for the first time via *in situ* combustion synthesis by employing tetrabutylammonium bromide (TBAB) as fuel, reactant, and source of ionic liquid simultaneously, and urea as assistant fuel. The formation of heterojunction by introduction of Bi_2O_3 decreases the electron-hole separation efficiency of layer structured $\text{Bi}_3\text{O}_4\text{Br}$ and the oxygen activation ability. $\text{Bi}_3\text{O}_4\text{Br}$ exhibits much higher molecular oxygen activation performance to form superoxide anion radicals ($\cdot\text{O}_2^-$) than Bi_2O_3 partly because of the existence of surface oxygen vacancies and thus strengthening the O_2 adsorption ability. However, the as-prepared heterojunctions exhibit enhanced photocatalytic activity in degradation of the orange (MO) and colorless pollutant phenol. The reaction rate constant in degradation of MO over $\text{Bi}_3\text{O}_4\text{Br}/\alpha\text{-Bi}_2\text{O}_3$ heterojunction containing 61 wt% $\text{Bi}_3\text{O}_4\text{Br}$ and 39 wt% Bi_2O_3 is 11.6 and 5.2 times that of pristine Bi_2O_3 and $\text{Bi}_3\text{O}_4\text{Br}$, respectively, which can be attributed to the existence of holes on Bi_2O_3 at more positive potential resulted from the hybridizing with

$\text{Bi}_3\text{O}_4\text{Br}$. The present work may provide a new insight into constructing heterostructured nanomaterials with desirable energy band position and deepen the understanding on the role of holes in the direct photocatalytic oxidation process.

Acknowledgments

We thank the financial supports from National Natural Science Foundation of China (No. 21776059, 21376061), Natural Science Foundation for Distinguished Young Scholar of Hebei Province (B2015208010), Scientific Research Foundation for High-Level Talent in University of Hebei Province (GCC2014057), and Foundation for the Returned Overseas Chinese Scholars of Hebei Province (CL201609).

Appendix A. Supplementary data

Supplementary data associated with this article can be found, in the online version, at <http://dx.doi.org/10.1016/j.apcatb.2017.11.046>.

References

- R.J. Hou, Y. Gao, H.J. Zhu, G.X. Yang, W.H. Liu, Y.N. Huo, Z.L. Xie, H.X. Li, *Chem. Eng. J.* 317 (2017) 386–393.
- Y.L. Li, Y.M. Liu, J.S. Wang, E. Uchaker, Q.F. Zhang, S.B. Sun, Y.X. Huang, J.Y. Li, G.Z. Cao, *J. Mater. Chem. A* 1 (2013) 7949–7956.
- R. van Grieken, J. Marugán, C. Sordo, P. Martínez, C. Pablos, *Appl. Catal. B: Environ.* 93 (2009) 112–118.
- P. Zhang, T. Tachikawa, M. Fujiitsuka, T. Majima, *ChemSusChem* 9 (2016) 617–623.
- A. Hameed, M. Aslam, Iqbal M.I. Ismail, S. Chandrasekaran, M.W. Kadi, M.A. Gondal, *Appl. Catal. B* 160 (2014) 227–239.
- C. Wang, K. Maeda, A. Thomas, K. Takanabe, G. Xin, J.M. Carlsson, K. Domen, M. Antonietti, *Nat. Mater.* 8 (2009) 76–80.
- T. Saison, N. Chemin, C. Chaneac, O. Durupthy, V. Ruaux, L. Mariey, F. Mauge, P. Beaumier, J.P. Jolivet, *J. Phys. Chem. C* 115 (2011) 5657–5666.
- R.P. Xiao, C. Hu, C.L. Liu, C. Xing, X.X. Qian, J.M. Zuo, L.S. Nan, *Appl. Catal. B: Environ.* 140 (2013) 433–443.
- R.G. Li, F.X. Zhang, D.G. Wang, J.X. Yang, M.R. Li, J. Zhu, X. Zhou, H.X. Han, C. Li, *Nature Commun.* 4 (2013) 1432.
- H.W. Huang, K. Xiao, T.R. Zhang, F. Dong, Y.H. Zhang, *Appl. Catal. B: Environ.* 203 (2017) 879–888.
- J.G. Hou, S.Y. Cao, Y.Z. Wu, F. Liang, Y.F. Sun, Z.S. Lin, L.C. Sun, *Nano Energy* 32 (2017) 359–366.
- S.Q. Jiang, L. Wang, W.C. Hao, W.X. Li, H.J. Xin, W.W. Wang, T.M. Wang, *J. Phys. Chem. C* 119 (2015) 14094–14101.
- Y. Xu, J. Song, F. Chen, X.F. Wang, H.G. Yu, J.G. Yu, *RSC Adv.* 6 (2016) 65902–65910.
- Q. Sun, X.R. Jia, X.F. Wang, H.G. Yu, J.G. Yu, *Dalton Trans.* 44 (2015) 14532–14539.
- J. Wang, W.Y. Yang, F.T. Li, J. Zhao, R.H. Liu, S.J. Liu, B. Li, *J. Hazard. Mater.* 292 (2015) 126–136.
- J. Tian, P. Hao, N. Wei, H.Z. Cui, H. Liu, *ACS Catal.* 5 (2015) 4530–4536.
- H.F. Li, H.T. Yu, X. Quan, S. Chen, H.M. Zhao, *Adv. Funct. Mater.* 25 (2015) 3074–3080.
- M. Palmai, E.M. Zahran, S. Angaramo, S. Balint, Z. Paszti, M.R. Knecht, L.G. Bachas, *J. Mater. Chem. A* 5 (2017) 529–534.
- N. Li, R.K. Huang, Y.H. Hu, Y.J. Chen, W.J. Liu, R.S. Yuan, Z.H. Li, *Inorg. Chem.* 51 (2012) 6245–6250.
- O.F. Lopes, K.T.G. Carvalho, W. Avansi, C. Ribeiro, *J. Phys. Chem. C* 121 (2017) 13747–13756.
- Y.F. Liu, W.Q. Yao, D. Liu, R.L. Zong, M. Zhang, X.G. Ma, Y.F. Zhu, *Appl. Catal. B: Environ.* 163 (2015) 547–553.
- W.W. He, H.K. Kim, W.G. Wamer, D. Melka, J.H. Callahan, J.J. Yin, *J. Am. Chem. Soc.* 136 (2014) 750–757.
- H. Wang, S.C. Chen, D.Y. Yong, X.D. Zhang, S. Li, W. Shao, X.S. Sun, B.C. Pan, Y. Xie, *J. Am. Chem. Soc.* 139 (2017) 4737–4742.
- F.T. Li, X.J. Wang, Y. Zhao, J.X. Liu, Y.J. Hao, R.H. Liu, D.S. Zhao, *Appl. Catal. B: Environ.* 144 (2014) 442–453.
- H.B. Fu, C.S. Pan, W.Q. Yao, Y.F. Zhu, *J. Phys. Chem. B* 109 (2005) 22432–22439.
- A. Fujishima, X.T. Zhang, C. R. Chim. 9 (2006) 750–760.
- S. Kim, W. Choi, *Environ. Sci. Technol.* 36 (2002) 2019–2025.
- J. Schneider, M. Matsuka, M. Takeuchi, J.L. Zhang, Y. Horiuchi, M. Anpo, D.W. Bahnemann, *Chem. Rev.* 114 (2014) 9919–9986.
- Z.H. Zhang, F.L. Ai, L.Z. Jia, J. Zhang, *J. Phys. Chem. C* 112 (2008) 747–753.
- H. Li, J. Shang, Z.H. Ai, L.Z. Zhang, *J. Am. Chem. Soc.* 137 (2015) 6393–6399.
- J.L. Wang, Y. Yu, L.Z. Zhang, *Appl. Catal. B: Environ.* 136 (2013) 112–121.
- F.T. Li, Q. Wang, J.R. Ran, Y.J. Hao, X.J. Wang, D.S. Zhao, S.Z. Qiao, *Nanoscale* 7 (2015) 1116–1126.
- F.T. Li, Y. Liu, Z.M. Sun, R.H. Liu, C.G. Kou, Y. Zhao, D.S. Zhao, *Mater. Lett.* 65 (2011) 406–408.
- F.T. Li, Y. Liu, Z.M. Sun, Y. Zhao, R.H. Liu, L.J. Chen, D.S. Zhao, *Catal. Sci. Technol.* 2 (2012) 1455–1462.
- F.T. Li, J.R. Ran, M. Jaroniec, S.Z. Qiao, *Nanoscale* 7 (2015) 17590–17610.
- J. Bai, L. Wang, Y.J. Wang, W.Q. Yao, Y.F. Zhu, *Appl. Catal. B: Environ.* 152 (2014) 262–270.
- H. Zhang, L.H. Guo, L.X. Zhao, B. Wan, Y. Yang, *J. Phys. Chem. Lett.* 6 (2015) 958–963.
- J.L. Zhang, L.S. Zhang, X.F. Shen, P.F. Xu, J.S. Liu, *CrystEngComm* 18 (2016) 3856–3865.
- S.J. Liang, R.W. Liang, L.R. Wen, R.S. Yuan, L. Wu, X.Z. Fu, *Appl. Catal. B: Environ.* 125 (2012) 103–110.
- F.T. Li, Y. Zhao, Y.J. Hao, X.J. Wang, R.H. Liu, D.S. Zhao, D.M. Chen, *J. Hazard. Mater.* 239 (2012) 118–127.
- C. Song, X. Wang, J. Zhang, X. Chen, C. Li, *Appl. Surf. Sci.* 425 (2017) 788–795.
- T. Jesty, K.S. Ambili, S. Radhika, *Catal. Today* (2017), <http://dx.doi.org/10.1016/j.cattod.2017.06.029>.
- F. Rouquerol, J. Rouquerol, K. Sing, *Adsorption by Powders and Porous Solids: Principles, Methodology, and Applications*, Academic Press, San Diego, 1999.
- H.P. Zhang, M.K. Lü, S.W. Liu, Z.L. Xiu, G.J. Zhou, Y.Y. Zhou, Z.F. Qiu, A.Y. Zhang, Q. Ma, *Surf. Coat. Technol.* 202 (2008) 4930–4934.
- D.S. Kong, *Langmuir* 24 (2008) 5324–5331.
- Y. Hou, F. Zuo, A. Dagg, P.Y. Feng, *Angew. Chem. Int. Ed.* 52 (2013) 1248–1252.
- S.J. Hong, S. Lee, J.S. Jang, J.S. Lee, *Energy Environ. Sci.* 4 (2011) 1781–1787.
- R. Saito, Y. Miseki, K. Sayama, *Chem. Commun.* 48 (2012) 3833–3835.
- S.X. Weng, B.B. Chen, L.Y. Xie, Z.Y. Zheng, P. Liu, *J. Mater. Chem. A* 1 (2013) 3068–3075.
- L.Z. Zhang, T.F. Zhang, D.J. Xie, J. Wang, *J. Phys. Chem. C* 113 (2009) 7371–7378.
- M.Y. Zhang, C.L. Shao, J.B. Mu, X.M. Huang, Z.Y. Zhang, Z.C. Guo, P. Zhang, Y.C. Liu, *J. Mater. Chem.* 22 (2012) 577–584.
- L. Kong, Z. Jiang, H.H. Lai, R.J. Nicholls, T.C. Xiao, M.O. Jones, P.P. Edwards, *J. Catal.* 293 (2012) 116–125.
- M.M. Khan, S.A. Ansari, D. Pradhan, M.O. Ansari, D.H. Han, J. Lee, M.H. Cho, *J. Mater. Chem. A* 2 (2014) 637–644.
- B.H.J. Bielski, G.G. Shiu, S. Bajuk, *J. Phys. Chem.* 84 (1980) 830–833.
- M. Quinones, Y. Zhang, P. Riascos, H.M. Hwang, W.G. Aker, X. He, R.M. Gao, *Photochem. Photobiol.* 90 (2014) 374–379.
- Y.H. Lv, Y.Y. Zhu, Y.F. Zhu, *J. Phys. Chem. C* 117 (2013) 18520–18528.
- R.D. Zhang, H.S. Alamdari, S. Kalilaguine, *J. Catal.* 242 (2006) 241–253.
- K. Xie, N. Umezawa, N. Zhang, P. Reunchan, Y.J. Zhang, J.H. Ye, *Energy Environ. Sci.* 4 (2011) 4211–4219.
- S. Li, L.B. Hou, L.J. Zhang, L.P. Chen, Y.H. Lin, D.J. Wang, T.F. Xie, *J. Mater. Chem. A* 3 (2015) 17820–17826.
- H.L. Wang, L.S. Zhang, Z.G. Chen, J.Q. Hu, S.J. Li, Z.H. Wang, J.S. Liu, X.C. Wang, *Chem. Soc. Rev.* 43 (2014) 5234–5244.
- S.L. Wang, L.L. Wang, W.H. Ma, D.M. Johnson, Y.F. Fang, M.K. Jia, Y.P. Huang, *Chem. Eng. J.* 259 (2015) 410–416.
- Z.H. Ai, J.L. Wang, L.Z. Zhang, *Chin. J. Catal.* 36 (2015) 2145–2154.